Energy Storage Materials 30 (2020) 98–103

Contents lists available at ScienceDirect

Energy Storage Materials

journal homepage: www.elsevier.com/locate/ensm

Single crystal cathodes enabling high-performance all-solid-state lithium-ion batteries

Changhong Wang [a], Ruizhi Yu [a], Sooyeon Hwang [b], Jianwen Liang [a], Xiaona Li [a], Changtai Zhao [a], Yipeng Sun [a], Jiwei Wang [a], Nathaniel Holmes [a], Ruying Li [a], Huan Huang [c], Shangqian Zhao [d], Li Zhang [d], Shigang Lu [d], Dong Su [b,**], Xueliang Sun [a,*]

[a] Department of Mechanical and Materials Engineering, University of Western Ontario, 1151 Richmond St, London, Ontario, N6A 3K7, Canada
[b] Center for Functional Nanomaterials, Brookhaven National Laboratory, Upton, NY, 11973, United States
[c] Glabat Solid-State Battery Inc., 700 Collip Circle, London, ON, N6G 4X8, Canada
[d] China Automotive Battery Research Institute Co., Ltd., 5th Floor, No. 43, Mining Building, North Sanhuan Middle Road, Haidian District Beijing, P.C, 100088, China

ARTICLE INFO

Keywords:
Single-crystal $LiNi_{0.5}Mn_{0.3}Co_{0.2}O_2$
Superior rate performance
Li^+ diffusion coefficient
All-solid-state lithium-ion batteries

ABSTRACT

All-solid-state lithium-ion batteries (ASSLIBs) are receiving significant attention owing to their improved safety and energy density over liquid counterparts. However, single-crystal cathodes have never been investigated in ASSLIBs. In this work, single-crystal $Li(Ni_{0.5}Mn_{0.3}Co_{0.2})O_2$ (SC-NMC532) is used as the cathode material for ASSLIBs, which exhibits 6–14 times higher Li^+ diffusion coefficient than polycrystalline $Li(Ni_{0.5}Mn_{0.3}Co_{0.2})O_2$ (PC-NMC532). As a result, SC-NMC532 exhibits an initial specific capacity of 156.4 $mAh.g^{-1}$ while PC-NMC532 shows an initial capacity of only 127.5 $mAh.g^{-1}$. After 150 cycles, SC-NMC532 retains the capacity of 94.5 $mAh.g^{-1}$. More impressively, under a high current density of 1.3 mA cm^{-2}, SC-NMC532 exhibits a capacity of 82 $mAh.g^{-1}$, much higher than that of PC-NMC532 (2.1 $mAh.g^{-1}$). This work demonstrates that single-crystal NMC cathodes could enable both high power density and high energy density of ASSLIBs.

1. Introduction

Rechargeable lithium-ion batteries (LIBs) are widely used in electric vehicles and portable electronic devices [1,2]. However, the use of flammable organic liquid electrolytes with narrow electrochemical windows presents safety challenges and places a constraint on the energy density of LIBs [3]. To eliminate safety concerns, replacing liquid electrolytes with inorganic solid-state electrolytes in LIBs is regarded as the ultimate solution. All-solid-state LIBs (ASSLIBs) also allow for increased energy density by employing bi-polar stacking technology and using high-voltage cathodes and lithium metal anodes [4–7]. Owing to the significant improvements in safety and energy density, ASSLIBs have attracted considerable attention in recent years [8–11].

Several challenges hinder the development of ASSLIBs, including (1) insufficient ionic conductivity of solid-state electrolytes [12], (2) large interfacial resistance due to poor solid-solid contact and detrimental interfacial reactions [13–16], and (3) poor rate performance due to slow lithium-ion (Li^+) kinetics in ASSLIBs [17–19]. With continuous efforts over the past decades, many solid-state electrolytes with high ionic conductivity have been developed. The ionic conductivities of solid-state sulfide electrolytes (SEs), $Li_{9.54}Si_{1.74}P_{1.44}S_{11.7}Cl_{0.3}$ (25 mS cm^{-1}) [4], $Li_{10}GeP_2S_{12}$ (LGPS, 12 mS cm^{-1}) [20], and $Li_7P_3S_{11}$ (17 mS cm^{-1}) [21] surpass even that of liquid electrolytes [22]. Sulfide-based ASSBs are therefore regarded as one of the most promising solid-state battery systems. To address the problem of large interfacial resistance, many soluble SEs have been reported which, when coated on cathode materials or infiltrated into the electrode sheet, significantly reduce the interfacial resistance between electrodes and SEs [23–29]. Besides, various interfacial buffer layers (i.e. $LiNbO_3$, $LiTaO_3$) have been developed to effectively prevent the interfacial reactions between oxide cathodes and SEs [30–33].

In contrast to the tremendous effort toward improving the ionic conductivity of SEs and suppressing interfacial resistance [33–36], less attention has been paid to the cathode material itself in the all-solid-state battery system [37]. In this work, we explore the electrochemical performance of single-crystal $Li(Ni_{0.5}Mn_{0.3}Co_{0.2})O_2$ (SC-NMC532) in

* Corresponding author.
** Corresponding author.
E-mail addresses: dsu@bnl.gov (D. Su), xsun9@uwo.ca (X. Sun).

https://doi.org/10.1016/j.ensm.2020.05.007
Received 24 March 2020; Received in revised form 29 April 2020; Accepted 4 May 2020
Available online 12 May 2020

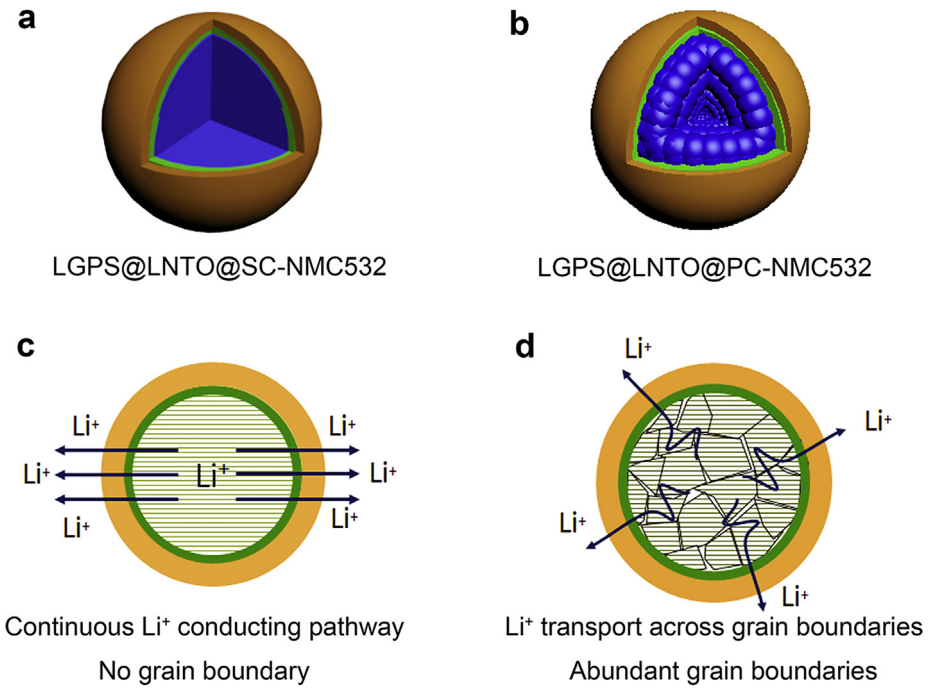

Figure 1. (a) Illustration of SC-NMC532 in SE-based ASSBs. (b) Illustration of PC-NMC532 in SE-based ASSBs. (c) A cross-sectional image of LGPS@LNTO@SC-NMC532, in which Li^+ has a continuous conducting pathway. (d) A cross-sectional image of LGPS@LNTO@PC-NMC532, in which Li^+ is transported across many grain boundaries.

SE-based ASSBs for the first time. It is found that the Li^+ diffusion coefficient of SC-NMC532 is 6–14 times higher than that of polycrystalline $Li(Ni_{0.5}Mn_{0.3}Co_{0.2})O_2$ (PC-NMC532). As a result, SC-NMC532 demonstrates a higher discharge capacity and significantly improved rate performance when compared to PC-NMC532. This work suggests that using single-crystal NMC cathodes could enable both high energy density and high-power density ASSLIBs.

2. Results and discussion

In conventional liquid cells, single-crystal cathode materials have shown substantial advantages over polycrystalline counterparts, such as particle integrity, thermal and high-voltage stability, and better safety [38]. However, single-crystal cathode materials have not been investigated yet in the solid-state battery system. Unlike the liquid cells, in which the liquid electrolyte can penetrate the pores of polycrystalline, the solid-state battery shows great challenge at the interfacial contact between cathodes and solid-state electrolytes. In general, the solid-state electrolyte can only contact the cathode materials on the surface through solid-solid contact. Polycrystalline cathodes possess many grain boundaries within a micro-spherical particle (Fig. 1b). In this case, Li^+ needs to pass through many grain boundaries before reaching the solid

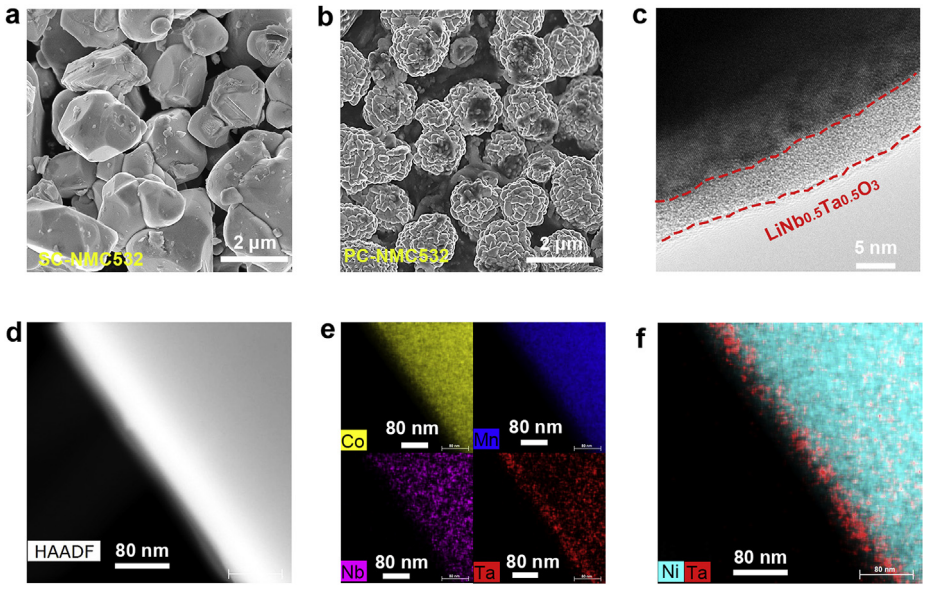

Fig. 2. Structural Characterization of LNTO@SC-NMC532 and LNTO@PC-NMC532. (a) An SEM image of LNTO@SC-NMC532. (b) An SEM image of LNTO@PC-NMC532. (c) HRTEM image of LNTO@SC-NMC532. (d) HAADF-STEM image of LNTO@SC-NMC532 and (e) STEM-EDX Co, Mn, Nb, and Ta elemental maps. (f) A combination of Ni and Ta elemental maps of LNTO@SC-NMC532 acquired with STEM-EDX.

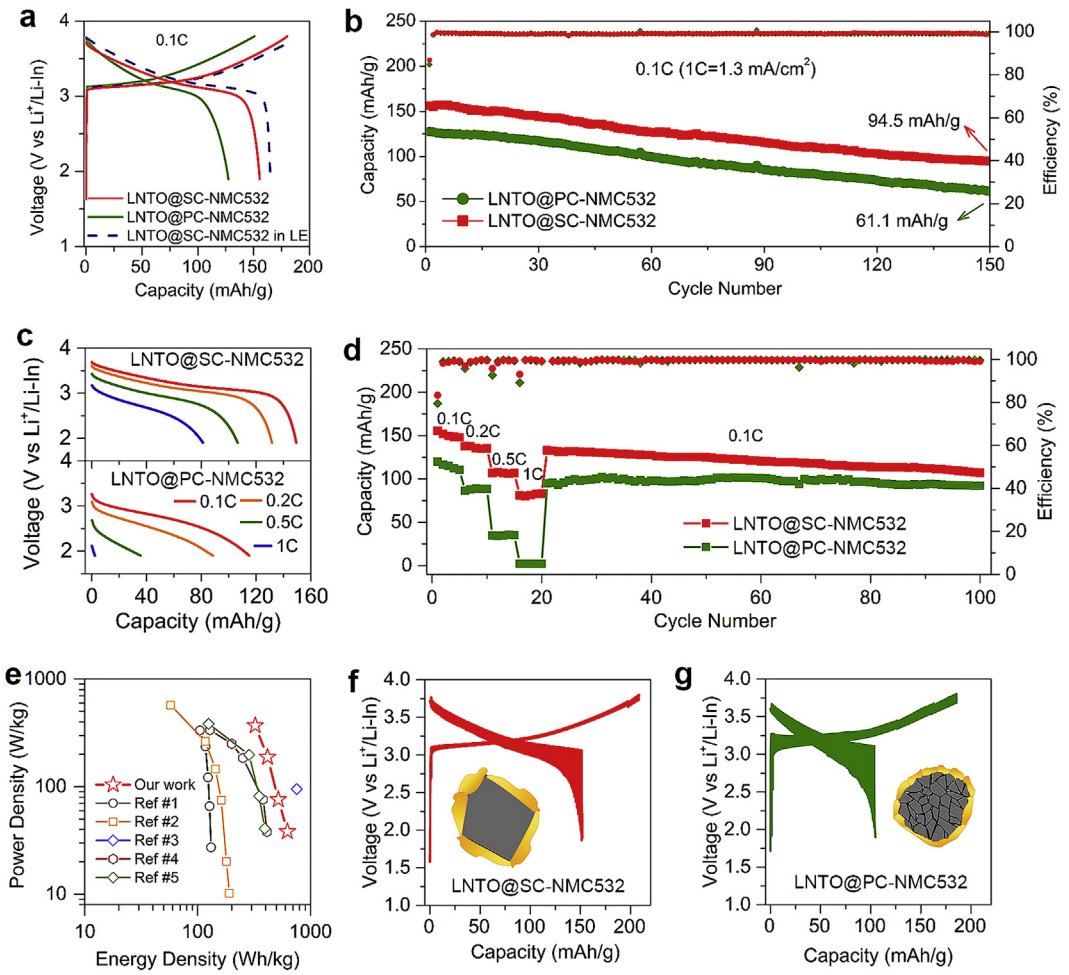

Fig. 3. Electrochemical Performance of LNTO@SC-NMC532 and LNTO@PC-NMC532. (a) Initial charge/discharge curves of LNTO@SC-NMC532, LNTO@PC-NMC532, and pristine SC-NMC532 in the conventional liquid electrolyte (LE). (b) Cycling stability of LNTO@SC-NMC532 and LNTO@PC-NMC532. (c) Discharge curves of LNTO@SC-NMC532 and LNTO@PC-NMC532 under various current densities. (d) Rate performance of LNTO@SC-NMC532 and LNTO@PC-NMC532. (e) The Ragone plots of LNTO@SC-NMC532-based ASSLIBs and previously reported ASSLIBs. (f) Charging/discharging GITT curves of LNTO@SC-NMC532. (g) Charging/discharging GITT curves of LNTO@PC-NMC532.

electrolyte (Fig. 1d). In contrast, single-crystal cathodes do not contain grain boundaries inside one particle (Fig. 1a), thus providing continuous Li^+ conduction pathways inside one particle (Fig. 1c). Therefore, the single-crystal cathode is believed to show faster Li^+ kinetics in solid-state batteries than the polycrystalline cathode.

To verify this assumption, SC-NMC532 (d_{50} = 3.8 μm) and PC-NMC532 (d_{50} = 4.2 μm) with the similar particle size were obtained and investigated in all-solid-state batteries (Fig. S1) [39]. To fairly compare their electrochemical performance difference, an interfacial layer of $LiNbTaO_3$ (LNTO) was therefore inserted between the NMC532 and SE to avoid the interfacial reactions. Scanning electron microscopy (SEM) images of LNTO-coated SC-NMC532 (LNTO@SC-NMC532) and LNTO-coated NMC532 (LNTO@PC-NMC532) are presented in Fig. 2a and b respectively. The SC-NMC532 samples are single particles with a diameter of about 2–5 μm while the PC-NMC532 samples are secondary microspheres with the same diameter. The thickness of the LNTO interfacial coating layer was about 7 nm, as revealed by the scanning transmission electron microscopy (STEM) image in Fig. 2c. To confirm the uniformity of the LNTO coating, SEM-energy dispersive X-ray spectroscopy elemental mappings of Ni, Co, Mn, Nb, and Ta are presented in Fig. S2. The uniform mapping of Nb and Ta on the SC-NMC532 implies the presence of a uniform LNTO layer. The high-angle annular dark-field (HAADF)-STEM image of LNTO-coated SC-NMC532 (Fig. 2d) and STEM-energy dispersive X-ray spectroscopy (EDX) elemental maps of Co, Mn, Nb, and Ta (Fig. 2e) also indicate a homogenous distribution of all elements. Besides, the combined map of Ni and Ta in the LNTO@SC-NMC532 shows that Ta has a strong signal at the edge (Fig. 2f), further suggesting that the LNTO was uniformly coated on the SC-NMC532. X-ray diffraction (XRD) patterns of LNTO@SC-NMC532 and LNTO@PC-NMC532 are compared in Fig. S3. No LNTO diffraction patterns are detected, indicating that the LNTO coating is amorphous. Interestingly, the (104) peak for SC-NMC532 at 44.6° is split, a typical characteristic of single-crystal NMC cathodes caused by the separation of $K_{\alpha1}$ and $K_{\alpha2}$ reflected from the (104) lattice plane in SC-NMC532 [38,40,41]. The higher intensity of the (003) peak of LNTO@SC-NMC532 than that of LNTO@PC-NMC532 implies more continuous Li^+ conduction pathways along the (003) plane in SC-NMC532. Furthermore, the electrochemical performance of LNTO@SC-NMC532 and LNTO@PC-NMC532 were examined using liquid cells. As shown in Fig. S4, the initial discharge capacities of both LNTO@SC-NMC532 and LNTO@PC-NMC532 are approximately 165 $mAh.g^{-1}$ at 0.1C (1C = 1.3 $mA\ cm^{-2}$). Besides, both of them exhibit very stable cycling performance.

To evaluate their performance in all-solid-state batteries, $Li_{10}GeP_2S_{12}$ (LGPS) with a high ionic conductivity of 3.5×10^{-3} S cm^{-1} was chosen as the SE in this study (Fig. S5). The detailed experimental procedure can be found in the supporting information. The electrochemical performance of LNTO@SC-NMC532 and LNTO@PC-NMC532 in SE-based ASSLIBs was first investigated under a current density of 0.1C (1C = 1.3 $mA\ cm^{-2}$).

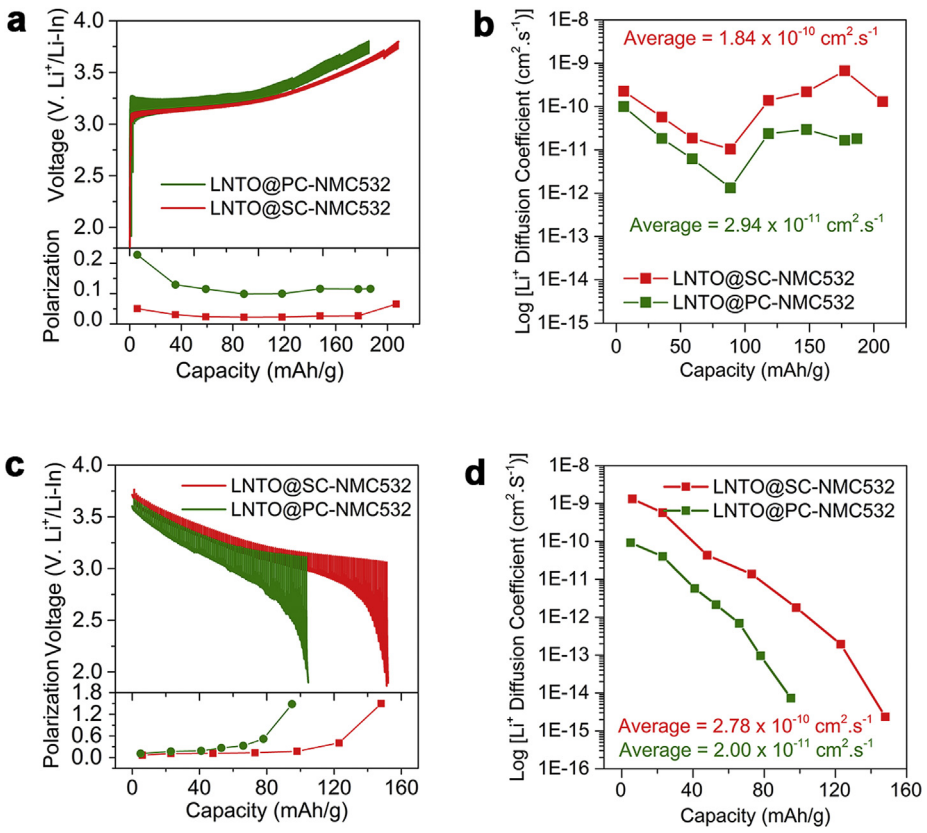

Fig. 4. Quantification of Li^+ diffusion coefficients of SC-NMC532 and PC-NMC532 during the initial charge/discharge process. (a) Comparison of the initial GITT charge curves and corresponding polarization curves. (b) Li^+ diffusion coefficients of LNTO@SC-NMC532 and LNTO@PC-NMC532 at different charge states. (c) Comparison of initial GITT discharge curves and corresponding polarization curves. (d) Li^+ diffusion coefficients of LNTO@SC-NMC532 and LNTO@PC-NMC532 at different discharge states.

LNTO@SC-NMC532 demonstrated a charge capacity of 179.9 mAh.g^{-1} and a discharge capacity of 156.4 mAh.g^{-1} with an initial coulombic efficiency of 86.9%. Comparatively, LNTO@PC-NMC532 displayed a discharge capacity of only 111.9 mAh.g^{-1}. Furthermore, the polarization voltage between the charge and the discharge curve of LNTO@SC-NMC532 is significantly smaller than that of LNTO@PC-NMC532, indicating that SC-NMC532 possesses faster Li^+ kinetics than PC-NMC532. After the 1st charging, LNTO@SC-NMC532 and LNTO@PC-NMC532 electrodes were checked by SEM (Fig. S6). Lots of cracks were observed on the LNTO@SC-NMC532 electrode after 1st charging, which is associated with the extremely volume shrinking of SC-NMC532 particles upon charging. Comparatively, the cracks on the LNTO@PC-NMC532 electrode is much smaller, because the PC-NMC532 particles could be fully charged, thus the corresponding volume shrinking is not as phenomenal as that of SC-NMC532. Furthermore, electrochemical impedance spectroscopy (EIS) analysis (Fig. S7) reveals interfacial resistance between LNTO@SC-NMC532 and LGPS is 112 Ω, which is slightly lower than that of LNTO@PC-NMC532 (127 Ω). The EIS analysis confirms the interfacial reaction between the cathode particles and LGPS is successfully prevented by LNTO.

Fig. 3b displays the cycling stability of LNTO@SC-NMC532 and LNTO@PC-NMC532. After 150 cycles, the LNTO@SC-NMC532 retains a specific capacity of 94.5 mAh.g^{-1} while LNTO@PC-NMC532 retains a specific capacity of only 61.1 mAh.g^{-1}. The corresponding decay rate of LNTO@SC-NMC532 is 0.35%, which is slightly lower than that of LNTO@PC-NMC532 (0.44%). The good cycling stability indicates that the interfacial LNTO coating effectively suppresses interfacial reactions. It should be mentioned that small-size PC-NMC532 exhibit higher capacity than large-size PC-NMC532 (Fig. S8), which is in good agreement with previous reports [39]. With the same particle size, SC-NMC532 shows higher active material utilization than PC-NMC532. The cyclic voltammetry (CV) profiles for LNTO@SC-NMC532 and LNTO@PC-NMC532 clearly show the redox peaks of Ni^{2+}/Ni^{4+} and Ni^{3+}/Ni^{4+} at around 3.3 V (vs. Li^+/Li–In) (Fig. S9). The overlapping of the oxidation/reduction peaks implies that LNTO@SC-NMC532 has good electrochemical reversibility in SE-based ASSLIBs. The peak currents of LNTO@SC-NMC532 are higher than those of LNTO@ PC-NMC532, and the polarization of LNTO@SC-NMC532 is less than that of LNTO@PC-NMC532. These findings are consistent with the conclusions derived from the charge/discharge curves in Fig. 3a.

The rate performance of LNTO@SC-NMC532 and LNTO@PC-NMC532 from 0.1C to 1C is presented in Fig. 3d and the corresponding discharge curves at various C-rates are depicted in Fig. 3c. LNTO@PC-NMC532 cannot be discharged at 1C due to significant voltage hysteresis (Fig. 3e), while LNTO@SC-NMC532 shows a discharge capacity of 82 mAh.g^{-1} at 1C. It should be mentioned that the inferior rate-performance of polycrystalline NMC cathodes as tabulated in Table S1, has been reported before [18,42,43]. Fig. 3e displays the Ragone plots of LNTO@SC-NMC532-based ASSLIBs and previously reported promising ASSLIBs at room temperature. Detailed references are listed in Table S2. Obviously, LNTO@SC-NMC532-based ASSLIBs offer the highest energy density and power density, suggesting that the high theoretical power density of ASSLIBs will be more readily realized by using single-crystal NMC cathodes instead of polycrystalline.

The disparity in rate-performance between LNTO@SC-NMC532 and LNTO@PC-NMC532 strongly suggests that LNTO@SC-NMC532 has faster Li^+ kinetics than LNTO@PC-NMC532 in ASSLIBs. To quantify the Li^+ diffusion coefficients, both LNTO@SC-NMC532 and LNTO@PC-NMC532 were tested during the initial charge/discharge process using the galvanostatic intermittent titration technique (GITT) (Fig. 3f and g). Both the polarization voltages and Li^+ diffusion coefficients of LNTO@SC-NMC532 and LNTO@PC-NMC532 are calculated based on the initial charge and discharge process separately and discussed in Fig. 4.

Based on the GITT results, the Li^+ diffusion coefficient can be calculated with the equation [23,32]:

$$D_{Li^+} = \frac{4}{\pi\tau}\left(\frac{m_{NMC532}V_{NMC532}}{M_{NMC532}S}\right)^2\left(\frac{\Delta E_s}{\Delta E_\tau}\right)^2 \quad (1)$$

where τ is the relaxation time (2 h), m_{NMC532} is the actual mass of SC-NMC532 in the electrode composite, V_{NMC532} is the molar volume of SC-NMC532 (20.73 $cm^3\ mol^{-1}$), M_{NMC532} is the molar mass of the host materials SC-Li($Ni_{0.5}Mn_{0.3}Co_{0.2}$)O_2 (96.58 g mol^{-1}), ΔE_s is the steady-voltage change after 2 h of relaxation and ΔE_τ is the change in the transient-voltage change after a 5 min discharge process at 0.13 mA cm^{-2}.

Fig. 4a compares the GITT curves and electrochemical polarization of LNTO@SC-NMC532 and LNTO@PC-NMC532 during the charging process. The electrochemical polarization of LNTO@SC-NMC532 is less than 50 mV while that of LNTO@PC-NMC532 is over 110 mV. The average Li^+ diffusion coefficient of LNTO@SC-NMC532 is 1.84×10^{-10} cm [2].s^{-1} during the initial charge process, 6.25 times higher than that of LNTO@PC-NMC532 (2.94×10^{-11} cm [2].s^{-1}) (Fig. 4b). Fig. 4c shows the GITT profiles and polarization voltages of LNTO@SC-NMC532 and LNTO@PC-NMC532 during the initial discharging process. The discharging polarization voltage of LNTO@SC-NMC532 (<180 mV) is also smaller than that of PC-NMC532 (~300 mV). The increased polarization at the end of the discharge process is due to the saturation of Li^+ sites in the NMC532 crystal structure [32]. The average Li^+ diffusion coefficient for LNTO@SC-NMC532 (2.78×10^{-10} cm [2].s^{-1}) during the discharge process is almost 13.9 times higher than that of LNTO@PC-NMC532 (2.00×10^{-11} cm [2].s^{-1}) (Fig. 4d). Overall, LNTO@SC-NMC532 exhibits a Li^+ diffusion coefficient of 6–14 times higher than LNTO@PC-NMC532 in ASSLIBs. Therefore, single-crystal NMC cathodes have a greater potential to simultaneously enable high energy density and power density of ASSLIBs.

3. Conclusion

In summary, we systematically compared the electrochemical performance of SC-NMC532 and PC-NMC532 in SE-based ASSLIBs. SC-NMC532 exhibits a Li^+ diffusion coefficient of 6–14 times higher than PC-NMC532. Consequently, SC-NMC532 exhibits an initial specific capacity of 156.4 mAh.g^{-1} and retains a specific capacity of 94.5 mAh.g^{-1} after 150 cycles. More importantly, SC-NMC532 exhibits a specific capacity of 82 mAh.g^{-1} under a high current density of 1.3 mA cm^{-2} while PC-NMC532 only shows 2.1 mAh.g^{-1}. This work demonstrates that single-crystal NMC cathodes have bigger advantages than polycrystalline counterparts toward high-performance ASSLIBs.

Author contributions

C. W. and X. Sun conceived the idea. C. W. designed all the experiments and electrochemical characterizations. R. Yu helped with cathode material synthesis. S. H. and D. S. helped with TEM characterization and analysis. J. L. and X. L. interpreted the experimental results. C. Z., Y. S., and J. W. discussed all the experimental results. N. H. polished the language. R. L helped with purchasing all the chemicals. C. W. wrote the manuscript. All the authors discussed the results and commented on the manuscript. The whole project was supervised by X. S.

Declaration of competing interest

The authors declare that they have no known competing financial interests or personal relationships that could have appeared to influence the work reported in this paper.

CRediT authorship contribution statement

Changhong Wang: Conceptualization, Investigation, Writing - original draft. **Ruizhi Yu:** Investigation. **Sooyeon Hwang:** Formal analysis. **Jianwen Liang:** Formal analysis. **Xiaona Li:** Formal analysis. **Changtai Zhao:** Formal analysis. **Yipeng Sun:** Formal analysis. **Jiwei Wang:** Formal analysis. **Nathaniel Holmes:** Writing - review & editing. **Ruying Li:** Resources. **Huan Huang:** Formal analysis. **Shangqian Zhao:** Funding acquisition. **Li Zhang:** Funding acquisition. **Shigang Lu:** Funding acquisition. **Dong Su:** Supervision. **Xueliang Sun:** Supervision, Conceptualization.

Acknowledgements

This work was supported by Natural Sciences and Engineering Research Council of Canada (NSERC), Canada Research Chair Program (CRC), Canada Foundation for Innovation (CFI), Ontario Research Fund, China Automotive Battery Research Institute Co., Ltd, Glabat Solid-State Battery Inc., the Canada Light Source at University of Saskatchewan (CLS), Interdisciplinary Development Initiatives (IDI) by Western University, and University of Western Ontario. C.W. appreciates the funding support of the Mitacs Accelerate Fellowship. J.L. and X. L. thank the support of Mitacs Elevate Postdoctoral Fellowship. This research used resources of the Center for Functional Nanomaterials, which is a U.S. DOE Office of Science Facility at Brookhaven National Laboratory under Contract No. DE-SC0012704.

Appendix A. Supplementary data

Supplementary data to this article can be found online at https://doi.org/10.1016/j.ensm.2020.05.007.

References

[1] Y. Zhao, K. Zheng, X. Sun, Addressing interfacial issues in liquid-based and solid-state batteries by atomic and molecular layer deposition, Joule (2) (2018) 1–22.
[2] J.W. Choi, D. Aurbach, Promise and reality of post-lithium-ion batteries with high energy densities, Nat. Rev. Mater. 1 (2016) 16013.
[3] T. Famprikis, P. Canepa, J.A. Dawson, M.S. Islam, C. Masquelier, Fundamentals of inorganic solid-state electrolytes for batteries, Nat. Mater. 18 (12) (2019) 1278–1291.
[4] Y. Kato, S. Hori, T. Saito, K. Suzuki, M. Hirayama, A. Mitsui, M. Yonemura, H. Iba, R. Kanno, High-power all-solid-state batteries using sulfide superionic conductors, Nat. Energy 1 (2016) 16030.
[5] Y. Shen, Y. Zhang, S. Han, J. Wang, Z. Peng, L. Chen, Unlocking the energy capabilities of lithium metal electrode with solid-state electrolytes, Joule (2018).
[6] L. Liu, J. Xu, S. Wang, F. Wu, H. Li, L. Chen, Practical evaluation of energy densities for sulfide solid-state batteries, eTransportation 1 (2019) 100010.
[7] C. Wang, Y. Zhao, Q. Sun, X. Li, Y. Liu, J. Liang, X. Li, X. Lin, R. Li, K.R. Adair, L. Zhang, R. Yang, S. Lu, X. Sun, Stabilizing interface between Li10SnP2S12 and Li metal by molecular layer deposition, Nanomater. Energy 53 (2018) 168–174.
[8] A. Manthiram, X. Yu, S. Wang, Lithium battery chemistries enabled by solid-state electrolytes, Nat. Rev. Mater. 2 (2017) 16103.
[9] J. Li, C. Ma, M. Chi, C. Liang, N.J. Dudney, Solid electrolyte: the key for high-voltage lithium batteries, Adv Energy Mater 5 (4) (2015) 1401408.
[10] C. Wang, Q. Sun, Y. Liu, Y. Zhao, X. Li, X. Lin, M.N. Banis, M. Li, W. Li, K.R. Adair, D. Wang, J. Liang, R. Li, L. Zhang, R. Yang, S. Lu, X. Sun, Boosting the performance of lithium batteries with solid-liquid hybrid electrolytes: interfacial properties and effects of liquid electrolytes, Nanomater. Energy 48 (2018) 35–43.
[11] Y.-G. Lee, S. Fujiki, C. Jung, N. Suzuki, N. Yashiro, R. Omoda, D.-S. Ko, T. Shiratsuchi, T. Sugimoto, S. Ryu, J.H. Ku, T. Watanabe, Y. Park, Y. Aihara, D. Im, I.T. Han, High-energy long-cycling all-solid-state lithium metal batteries enabled by silver–carbon composite anodes, Nat. Energy (2020).
[12] Y. Wang, W.D. Richards, S.P. Ong, L.J. Miara, J.C. Kim, Y. Mo, G. Ceder, Design principles for solid-state lithium superionic conductors, Nat. Mater. 14 (10) (2015) 1026–1031.
[13] W.D. Richards, L.J. Miara, Y. Wang, J.C. Kim, G. Ceder, Interface stability in solid-state batteries, Chem. Mater. 28 (2016) 266–273.
[14] Y. Zhu, X. He, Y. Mo, First principles study on electrochemical and chemical stability of solid electrolyte–electrode interfaces in all-solid-state Li-ion batteries, J. Mater. Chem. 4 (9) (2016) 3253–3266.
[15] C. Wang, X. Li, Y. Zhao, M.N. Banis, J. Liang, X. Li, Y. Sun, K.R. Adair, Q. Sun, Y. Liu, F. Zhao, S. Deng, X. Lin, R. Li, Y. Hu, T.-K. Sham, H. Huang, L. Zhang, R. Yang, S. Lu, X. Sun, Manipulating interfacial nanostructure to achieve high-performance all-solid-state lithium-ion batteries, Small Methods 3 (10) (2019) 1900261.
[16] Q. Zhang, D. Cao, Y. Ma, A. Natan, P. Aurora, H. Zhu, Sulfide-based solid-state electrolytes: synthesis, stability, and potential for all-solid-state batteries, Adv. Mater. 31 (44) (2019) 1901131.
[17] F. Strauss, T. Bartsch, L. de Biasi, A.Y. Kim, J. Janek, P. Hartmann, T. Brezesinski, Impact of cathode material particle size on the capacity of bulk-type All-solid-state batteries, ACS Energy Lett (2018) 992–996.

[18] R. Koerver, I. Aygün, T. Leichtweiß, C. Dietrich, W. Zhang, J.O. Binder, P. Hartmann, W.G. Zeier, J. Janek, Capacity fade in solid-state batteries: interphase formation and chemomechanical processes in nickel-rich layered oxide cathodes and lithium thiophosphate solid electrolytes, Chem. Mater. 19 (2017) 5574–5582.
[19] N. Ohta, K. Takada, L. Zhang, R. Ma, M. Osada, T. Sasaki, Enhancement of the high-rate capability of solid-state lithium batteries by nanoscale interfacial modification, Adv. Mater. 18 (17) (2006) 2226–2229.
[20] N. Kamaya, K. Homma, Y. Yamakawa, M. Hirayama, R. Kanno, M. Yonemura, T. Kamiyama, Y. Kato, S. Hama, K. Kawamoto, A. Mitsui, A lithium superionic conductor, Nat. Mater. 10 (9) (2011) 682–686.
[21] H. Lee, P. Oh, J. Kim, H. Cha, S. Chae, S. Lee, J. Cho, Advances and prospects of sulfide all-solid-state lithium batteries via one-to-one Comparison with conventional liquid lithium ion batteries, Adv. Mater. 31 (29) (2019) 1900376.
[22] K. Xu, Nonaqueous liquid electrolytes for lithium-based rechargeable batteries, Chem. Rev. 104 (10) (2004) 4303–4418.
[23] K.H. Park, D.Y. Oh, Y.E. Choi, Y.J. Nam, L. Han, J.-Y. Kim, H. Xin, F. Lin, S.M. Oh, Y.S. Jung, Solution-processable glass LiI-Li4SnS4 superionic conductors for all-solid-state Li-ion batteries, Adv. Mater. 28 (9) (2016) 1874–1883.
[24] K.H. Park, Q. Bai, D.H. Kim, D.Y. Oh, Y. Zhu, Y. Mo, Y.S. Jung, Design strategies, practical considerations, and new solution processes of sulfide solid electrolytes for all-solid-state batteries, Adv. Energy Mater. 8 (18) (2018) 1800035.
[25] D.H. Kim, D.Y. Oh, K.H. Park, Y.E. Choi, Y.J. Nam, H.A. Lee, S.-M. Lee, Y.S. Jung, Infiltration of solution-processable solid electrolytes into conventional Li-ion-battery electrodes for all-solid-state Li-ion batteries, Nano Lett. 17 (5) (2017) 3013–3020.
[26] A. Sakuda, K. Kuratani, M. Yamamoto, M. Takahashi, T. Takeuchi, H. Kobayashi, All-solid-state battery electrode sheets prepared by a slurry coating process, J. Electrochem. Soc. 164 (12) (2017) A2474–A2478.
[27] Y.J. Nam, D.Y. Oh, S.H. Jung, Y.S. Jung, Toward practical all-solid-state lithium-ion batteries with high energy density and safety: comparative study for electrodes fabricated by dry- and slurry-mixing processes, J. Power Sources 375 (2018) 93–101.
[28] A. Miura, N.C. Rosero-Navarro, A. Sakuda, K. Tadanaga, N.H.H. Phuc, A. Matsuda, N. Machida, A. Hayashi, M. Tatsumisago, Liquid-phase syntheses of sulfide electrolytes for all-solid-state lithium battery, Nat. Rev. Chem. 3 (3) (2019) 189–198.
[29] C. Wang, K.R. Adair, J. Liang, X. Li, Y. Sun, X. Li, J. Wang, Q. Sun, F. Zhao, X. Lin, R. Li, H. Huang, L. Zhang, R. Yang, S. Lu, X. Sun, Solid-state plastic crystal electrolytes: effective protection interlayers for sulfide-based all-solid-state lithium metal batteries, Adv. Funct. Mater. 29 (26) (2019) 1900392.
[30] S.P. Culver, R. Koerver, W.G. Zeier, J. Janek, On the functionality of coatings for cathode active materials in thiophosphate-based all-solid-state batteries, Adv. Energy Mater. 9 (24) (2019) 1900626.
[31] Y. Xiao, L.J. Miara, Y. Wang, G. Ceder, Computational screening of cathode coatings for solid-state batteries, Joule 3 (2019) 1–24.
[32] C. Wang, J. Liang, S. Hwang, X. Li, Y. Zhao, K. Adair, C. Zhao, X. Li, S. Deng, X. Lin, X. Yang, R. Li, H. Huang, L. Zhang, S. Lu, D. Su, X. Sun, Unveiling the critical role of interfacial ionic conductivity in all-solid-state lithium batteries, Nanomater. Energy 72 (2020) 104686.
[33] X. Li, Q. Sun, Z. Wang, D. Song, H. Zhang, X. Shi, C. Li, L. Zhang, L. Zhu, Outstanding electrochemical performances of the all-solid-state lithium battery using Ni-rich layered oxide cathode and sulfide electrolyte, J. Power Sources 456 (2020) 227997.
[34] D.H.S. Tan, A. Banerjee, Z. Chen, Y.S. Meng, From nanoscale interface characterization to sustainable energy storage using all-solid-state batteries, Nat. Nanotechnol. 15 (3) (2020) 170–180.
[35] W.D. Jung, J.-S. Kim, S. Choi, S. Kim, M. Jeon, H.-G. Jung, K.Y. Chung, J.-H. Lee, B.-K. Kim, J.-H. Lee, H. Kim, Superionic halogen-rich Li-argyrodites using in situ nanocrystal nucleation and rapid crystal growth, Nano Lett. 20 (4) (2020) 2303–2309.
[36] J. Liang, N. Chen, X. Li, X. Li, K.R. Adair, J. Li, C. Wang, C. Yu, M. Norouzi Banis, L. Zhang, S. Zhao, S. Lu, H. Huang, R. Li, Y. Huang, X. Sun, Li10Ge(P1–xSbx)2S12 lithium-ion conductors with enhanced atmospheric stability, Chem. Mater. 32 (6) (2020) 2664–2672.
[37] S.H. Jung, U.-H. Kim, J.-H. Kim, S. Jun, C.S. Yoon, Y.S. Jung, Y.-K. Sun, Ni-rich layered cathode materials with electrochemo-mechanically compliant microstructures for all-solid-state Li batteries, Adv. Energy Mater. 10 (6) (2020) 1903360.
[38] J. Li, A.R. Cameron, H. Li, S. Glazier, D. Xiong, M. Chatzidakis, J. Allen, G.A. Botton, J.R. Dahn, Comparison of single crystal and polycrystalline LiNi0.5Mn0.3Co0.2O2 positive electrode materials for high voltage Li-ion cells, J. Electrochem. Soc. 164 (7) (2017) A1534–A1544.
[39] F. Strauss, T. Bartsch, L. de Biasi, A.Y. Kim, J. Janek, P. Hartmann, T. Brezesinski, Impact of cathode material particle size on the capacity of bulk-type All-solid-state batteries, ACS Energy Lett 3 (4) (2018) 992–996.
[40] H. Li, J. Li, X. Ma, J.R. Dahn, Synthesis of single crystal LiNi0.6Mn0.2Co0.2O2 with enhanced electrochemical performance for lithium ion batteries, J. Electrochem. Soc. 165 (5) (2018) A1038–A1045.
[41] J. Li, H. Li, W. Stone, R. Weber, S. Hy, J.R. Dahn, Synthesis of single crystal LiNi0.5Mn0.3Co0.2O2 for lithium ion batteries, J. Electrochem. Soc. 164 (14) (2017) A3529–A3537.
[42] H. Tsukasaki, M. Otoyama, Y. Mori, S. Mori, H. Morimoto, A. Hayashi, M. Tatsumisago, Analysis of structural and thermal stability in the positive electrode for sulfide-based all-solid-state lithium batteries, J. Power Sources 367 (2017) 42–48.
[43] M.A. Kraft, S. Ohno, T. Zinkevich, R. Koerver, S.P. Culver, T. Fuchs, A. Senyshyn, S. Indris, B.J. Morgan, W.G. Zeier, Inducing high ionic conductivity in the lithium superionic argyrodites Li6+xP1–xGexS5I for all-solid-state batteries, J. Am. Chem. Soc. 140 (47) (2018) 16330–16339.